

AD_____

Award Number: W81XWH-11-1-0232

TITLE: Feasibility of Prostate Cancer Diagnosis by Transrectal Photo-acoustic Imaging

PRINCIPAL INVESTIGATOR: Hanli Liu, Ph.D

CONTRACTING ORGANIZATION: The University of Texas at Arlington
Arlington, TX 76019

REPORT DATE: March 2013

TYPE OF REPORT: Annual report

PREPARED FOR: U.S. Army Medical Research and Materiel Command
Fort Detrick, Maryland 21702-5012

DISTRIBUTION STATEMENT: Approved for Public Release;
Distribution Unlimited

The views, opinions and/or findings contained in this report are those of the author(s) and should not be construed as an official Department of the Army position, policy or decision unless so designated by other documentation.

REPORT DOCUMENTATION PAGE			Form Approved OMB No. 0704-0188		
Public reporting burden for this collection of information is estimated to average 1 hour per response, including the time for reviewing instructions, searching existing data sources, gathering and maintaining the data needed, and completing and reviewing this collection of information. Send comments regarding this burden estimate or any other aspect of this collection of information, including suggestions for reducing this burden to Department of Defense, Washington Headquarters Services, Directorate for Information Operations and Reports (0704-0188), 1215 Jefferson Davis Highway, Suite 1204, Arlington, VA 22202-4302. Respondents should be aware that notwithstanding any other provision of law, no person shall be subject to any penalty for failing to comply with a collection of information if it does not display a currently valid OMB control number. PLEASE DO NOT RETURN YOUR FORM TO THE ABOVE ADDRESS.					
1. REPORT DATE (DD-MM-YYYY) T 8 2013		2. REPORT TYPE Annual report		3. DATES COVERED (From - To) F 8 2013 - F 8 2013	
4. TITLE AND SUBTITLE Feasibility of Prostate Cancer Diagnosis by Transrectal Photo-acoustic Imaging			5a. CONTRACT NUMBER		
			5b. GRANT NUMBER W81XH-11-1-0232		
			5c. PROGRAM ELEMENT NUMBER		
6. AUTHOR(S) Hanli Liu, Ph.D Professor of Bioengineering			5d. PROJECT NUMBER		
			5e. TASK NUMBER		
			5f. WORK UNIT NUMBER		
7. PERFORMING ORGANIZATION NAME(S) AND ADDRESS(ES) The University of Texas at Arlington Arlington, TX 76019			8. PERFORMING ORGANIZATION REPORT NUMBER		
9. SPONSORING / MONITORING AGENCY NAME(S) AND ADDRESS(ES) U.S. Army Medical Research and Materiel Command Fort Detrick, Maryland 21702-5012			10. SPONSOR/MONITOR'S ACRONYM(S)		
			11. SPONSOR/MONITOR'S REPORT NUMBER(S)		
12. DISTRIBUTION / AVAILABILITY STATEMENT Approved for public release; distribution unlimited					
13. SUPPLEMENTARY NOTES					
14. ABSTRACT There is no effective imaging tool currently available for prostate cancer detection; needle biopsy is the current practice for diagnosis of the disease, aiming randomly in the prostate. Transrectal ultrasound has been used as a guiding tool to direct tissue needle biopsy for prostate cancer diagnosis; it cannot be utilized for detecting prostate cancer due to lack of sensitivity. Recent studies show that the combination of light and ultrasound may lead to a new imaging device that can be used to provide cancer-sensitive, ultrasound images for prostate cancer detection. The goal of this study is to examine a new idea that combination of light and sound can lead to a better medical device so that doctors can clearly "see" harmful cancerous areas in the human prostate. The scientific basis for this idea is that when an organ is illuminated with light, cancer tissue will absorb more light and generate some heat. The light-generated heat, in turn, will be converted to sound wave and be "heard" by sound detectors. The cancerous sound waves will be plotted into images, allowing doctors "see" cancer better in the human prostate. The plan for the study includes two steps: (1) to setup the device and perform laboratory experiments using non-tissue samples, and (2) to calculate the measured data and thus to prove the new idea.					
15. SUBJECT TERMS Technology Development, optical spectroscopy, transrectal probe, optical biopsy, auto-fluorescence spectroscopy, fluorescence life-time measurement.					
16. SECURITY CLASSIFICATION OF: Unclassified			17. LIMITATION OF ABSTRACT	18. NUMBER OF PAGES	19a. NAME OF RESPONSIBLE PERSON Hanli Liu
a. REPORT X	b. ABSTRACT	c. THIS PAGE			19b. TELEPHONE NUMBER (include area code) (817) 272-2054

Table of Contents

SF 298.....	1
Table of Contents	2
1. Introduction.....	3
2. Body of the Report	3
3. Key Research Accomplishments and Reportable Outcomes	9
4. Conclusions	10
5. References.....	11
6. Published paper attached	12

2012-2013 Annual Progress Report

This report presents the specific aims and accomplishments of our prostate cancer research project during the year of funding sponsored by the US Department of the Army. It covers our activities from May 2012 to June 2013.

1. Summary of our Year 1 (2011-2012) research and development:

We have designed, implemented, and tested a frequency-domain photoacoustic imaging system using tissue-like phantoms. The imaging principle and data processing method have been presented and verified. The measured photoacoustic (PA) signal strength depends on the absorption coefficient, depth of the target, and the modulated light intensity of the laser diode. We have learned that appropriately processing the measured PA data and background interference is an important key to correctly display the PA images. The lateral spatial resolution of PA images depends on ultrasound frequencies and focal size of the ultrasound transducers. Although the current system has a low axial resolution (due to the adopted ultrasound transducer), the axial resolution can be improved by using a high numerical aperture ultrasound transducer [1] or by adopting a frequency-swept technique [2]. Our results and conclusion are accepted for a peer-reviewed publication [1], which is attached as an attachment.

In the meantime, however, we also learned that the frequency-domain photoacoustic imaging method developed by our approach has a severe limitation in sensing tissue signals deeper than 5 mm. Then, we tried to alter or modify our original idea by developing an integrated approach between ultrasound and optical tomography, namely, transrectal ultrasound-guided diffuse optical tomography (TRUS-DOT) for improved prostate cancer imaging. In the last 10-12 months, we have made great progress and obtained promising results using tissue-phantom experiments. We believe that our current development can lead to another innovative imaging method, which can correctly detect or identify aggressive prostate cancer tissue from non-aggressive tissues. In this report, we provide details on this modified/updated approach with computer simulations and experimental results.

2. Body of the Report

2.1 Hierarchical clustering to improve TRUS-DOT for prostate cancer imaging

Diffuse optical tomography (DOT) is a non-invasive imaging modality, which utilizes near infrared (NIR) light and provides blood-based absorption maps within the detected tissue volume interrogated by the optical optodes. When using multiple wavelengths, DOT is also capable of measuring chromosphere concentrations, such as oxy-hemoglobin, deoxy-hemoglobin, and water. Usage of DOT for breast cancer detection has been extensively studied. DOT instrumentation can be divided into three categories based on the principle of operation: (1) time resolved systems, (2) frequency domain systems and (3) continuous wave (CW) systems. Measurements in DOT can be made in the form of transmission, reflectance, or both. Time resolved systems rely on photon counting or gated imaging, which measures time of flight of photons through the tissue. However, these systems are very costly and bulky in comparison with CW systems. The frequency domain systems modulate the light source (e.g., laser diode) typically in the radio frequency range (e.g., 100 MHz) and measure the amplitude and phase shift of the detected signals. CW systems are the simplest, cost effective, and fastest in data collection; they can be made to image tissues at a video-rate. However, since CW systems measure only intensities of the reflected or transmitted light, they cannot separate the absorption and scattering effects of the tissue.

Despite of the instrumentation utilized, DOT has poor spatial resolution. Measurements in reflectance geometry are even worse in spatial resolution than in the transmission geometry. The cause that limits the spatial resolution of DOT is light scattering and diffusion in tissues, making DOT have to

solve an underdetermined and ill-posed inverse problem. One way to improve the spatial resolution is to couple DOT techniques with other imaging techniques, such as MRI, ultrasound (US), and others. This process is usually done by combining a *priori* information in the inversion procedure. In particular, a combined usage of TRUS with DOT could improve the accuracy in identifying prostate cancer 1-2 centimeters below the prostate surface, as studied previously [3]. However, this reported approach treated each anatomical region, such as the rectum wall, prostate gland, and prostate cancer lesion, to be homogenous and thus to be reconstructed with uniform optical properties within each region. However, the reconstructed images by the reported method [3] could be erroneous because of the fact that TRUS does not provide a clear or clean signature for prostate cancer. On the other hand, it has been demonstrated that the spatial resolution of reconstructed DOT images depends upon the number and locations of optical sources and detectors utilized. Given the limited space available in TRUS, the idea to incorporate more sources and detectors for a combined TRUS-DOT approach seems not to be very practical.

To solve the problems given above, we made new development in two aspects: (1) development of hierarchical clustering method (HCM) for improved contrast recovery and spatial resolution in DOT for prostate cancer imaging; (2) development of Trans-rectal compatible optical probe and instrumentation for prostate cancer imaging. First, in Section 2.2, we will explain the HCM procedure and demonstrate the capability of HCM using computer simulations. Then, in Section 2.3, we will explain the instrumentation utilized for trans-rectal compatible DOT and demonstrate the capability of HCM using laboratory phantoms.

2.2 Introduction, implementation, and Investigation of hierarchical clustering

Principle and algorithm of HCM

In standard practice, the equation used to iteratively update DOT image reconstruction is given by [4,5]

$$(J^T J + 2\lambda I)(\delta\mu_a) = J^T (y - F(\mu_a)) \quad (1)$$

where J is the Jacobin matrix (or called sensitivity matrix), I is the identity matrix, y is the measured data in a matrix form, F is the operator that generates the forward model for light propagation in tissues, μ_a is the vector of optical properties, and λ is the regularization parameter. Note that changes only in μ_a are considered in eq. (1), because our DOT measurement utilizes CW NIR light with an assumption that variation in light scattering across the medium is minimal.

In our HCM method, we divide the region of interest (ROI) (i.e., the prostate region) into several geometric clusters. We assume that each of the geometric clusters/units is homogeneous and has the same optical property. In this way, the computational domain could be partially heterogeneous since the domain may contain several geometric units. Specifically, the nodes in the mesh are tagged and separated into subsets ($GS_1, GS_2 \dots GS_I$) with respect to each unit. The Jacobian matrix in eq. (1) is then modified to J^* and is given by $J^* = JS$, where S matrix had a size of $NN \times NS$, where NN is the number of nodes within the specific unit/cluster and NS is the number of geometric clusters. The elements of S matrix are given by [5]:

$$S_{(i,j)} = \begin{cases} 1 & \text{if } i \in GS_i \\ 0 & \text{else} \end{cases} \quad (2)$$

At the end of each iteration, the solution vector is mapped back to each node using the following equation

$$\delta\mu_a = S(\delta\mu_a^*) \quad (3)$$

μ_a^* is a vector with optical properties of geometric clusters. When reconstructing two ROIs or clusters, such as background and anomaly, the background mesh was geometrically segmented in a heterogeneous fashion. For multiple clusters, we hierarchically implemented the proposed method by segmenting the region which is more prone to cancer, utilizing available prior spatial information. Specifically, we applied the proposed method in four steps, as shown in Fig. 1.

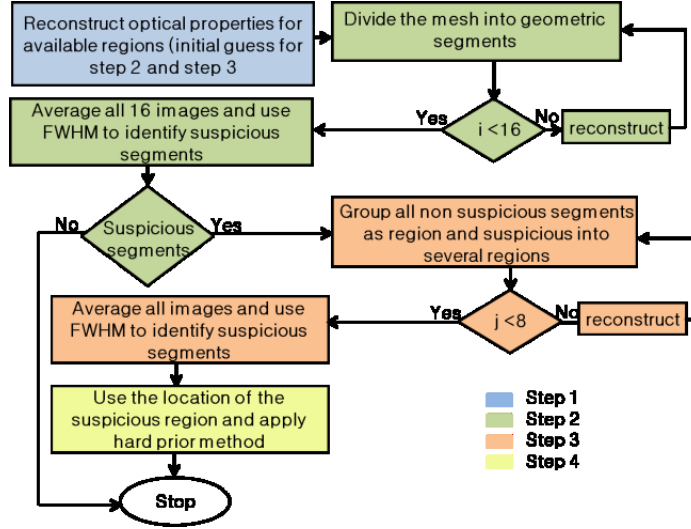


Figure 1: Flow chart indicating steps involved in HCM.

In step 1, the reconstruction is done based on TRUS images and the assumption of a homogeneous prostate. With such prior spatial information, the reconstructed μ_a values in both background and prostate region should be reasonably accurate with respect to the actual values. Then, the reconstructed μ_a values in available ROIs would serve as the initial guess in step 2 and step 3.

Step 2 of our method is dedicated to finding the probable locations of anomalies (i.e., prostate tumors). To achieve this, we geometrically divide the prostate region into several clusters, so the prostate tissue becomes a heterogeneous medium. However, without prior knowledge of suspicious locations, dividing the prostate into several clusters may result in mixing of suspicious tissue with normal prostate tissue and vice versa. In order to prevent this situation, we segment the prostate volume with different unit volume sizes iteratively. Specifically, we chose a unit volume as an initial segment size which is $1 \times 1 \times 1 \text{ cm}^3$ in each of the x, y and z dimensions. Then, we vary the volume size by increasing the linear length of the volume unit in each dimension iteratively. For example, an increase in length of 0.5 cm in only x direction gave rise to a unit volume of $1.5 \times 1 \times 1 \text{ cm}^3$, followed by the same length increase in only y or only z direction. In this way, we can generate 8 different unit volumes in three x, y, z directions, by increasing the linear length in only one dimension (x, y, z), or in two dimensions (xy, yz, xz), or in three dimensions (xyz) and the initial size.

The procedure is given as follows (see Fig. 1): (1) reconstruct an initial μ_a image with a starting base unit size (i.e., $1 \times 1 \times 1 \text{ cm}^3$), (2) save the reconstructed image, and go back and change the unit volume size (e.g., $1.5 \times 1 \times 1 \text{ cm}^3$ or $1.5 \times 1.5 \times 1 \text{ cm}^3$ or $1.5 \times 1.5 \times 1.5 \text{ cm}^3$) and reconstruct the image again (Step 2 in Fig.1). To be more comprehensive, we next increase our base unit volume from $1 \times 1 \times 1 \text{ cm}^3$ to $1.5 \times 1.5 \times 1.5 \text{ cm}^3$ and then to $2 \times 2 \times 2 \text{ cm}^3$, with the same length interval of 0.5 cm applied to increase the

base unit (e.g., $2 \times 1.5 \times 1.5 \text{ cm}^3$, $2 \times 2 \times 1.5 \text{ cm}^3$, or $2 \times 2 \times 2 \text{ cm}^3$). In this way, we are able to generate another set of 8 reconstructed images with varied base unit volumes, resulting in an overall 16 ($i=16$) images by the end of step two. (3) We average all of the reconstructed μ_a images to obtain the final image. (4) Next, we search for suspicious clusters using full width half maximum (FWHM) of the updated μ_a values within the prostate region. If no suspicious segment is identified, we conclude that the prostate has a low probability of having cancer.

In step 3, if some suspicious clusters in step 2 are seen, we then group all the non-suspicious clusters as one new single segment and subdivide the suspicious clusters into further smaller clusters. Now, the initial unit volume size used within the suspicious regions in step 3 is set to $0.5 \times 0.5 \times 0.5 \text{ cm}^3$. The procedure explained in step 2 is repeated here with a length variation of 0.25 cm in any one of three dimensions. Similar to step 2, the final reconstructed image of step 3 will be an average of the 8 images ($j=8$) obtained by varying the unit volume in 8 different fashions. FWHM of the μ_a values is still used to localize suspicious regions for further inspection with an improved spatial resolution.

Finally in step (4), the hard prior method was used to improve the optical properties of the suspicious regions identified in step 3. The initial guess here is the uniform initial guess as in step 1.

Computer simulations

To validate HCM, we performed computer simulations by considering a mesh, which was anatomically similar to a TRUS prostate image, consisting of four different ROIs, such as prostate, peri-prostate tissue, rectum wall and prostate tumors. Two spherical shaped inclusions were placed with a horizontal separation of 20 mm and a vertical depth of 20 mm from the surface of the rectal wall (Fig. 2). The rectum wall had a thickness of 5 mm and a curvature radius of 50 mm.

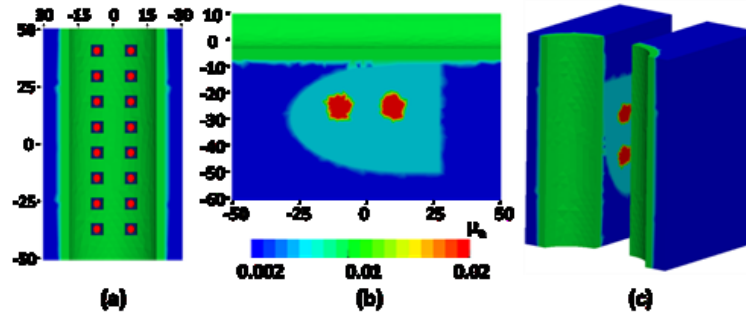


Figure 2: (a) Probe geometry used in the simulation; each optode is bifurcated to serve as a source and detector. (b) Two anomalies separated by 20 mm at a depth of 20 mm. (c) Mesh has been sliced isometric view to show the simulation geometry.

In step 1, as the prior location of prostate cancer is often not visible in TRUS images, we assumed homogeneous optical properties for all ROIs. A simulated TRUS-DOT probe was used, having 16 bifurcated optodes that could serve as both sources and detectors (Fig. 2a). The CW mode was utilized in the simulations; 1% random noise was added to the data to mimic the instrument noise. Simulated NIR data was computed along the rectum boundary using a FEM-based diffusion forward model with NIRFAST [6]. The first-step reconstruction was done using the initial guess of $\mu_a=0.01 \text{ mm}^{-1}$ to recover the optical property of the prostate (Fig. 3a). Then, the reconstructed data from the first step served as the initial guess for the second and third steps, as given in Section 2. All reconstructions would stop when the change in projection errors is less than 2% of the previous iteration. Next, the prostate tissue was divided into several clusters. As noted earlier, the final image obtained after step 2 was the average over 16 independently reconstructed images, as demonstrated in Fig. 3b. In this simulation, we found an estimated suspicious region, as marked by the dotted rectangle in Fig. 3b, using FWHM.

In step 3, the suspicious region identified in step 2 was further divided into smaller clusters. The final image of step 3 shown in Fig. 3c was the average over 8 reconstructed images. FWHM was used and resulted in two suspicious regions, which were treated as two individual regions and entered in the hard prior method for finer reconstruction in step 4.

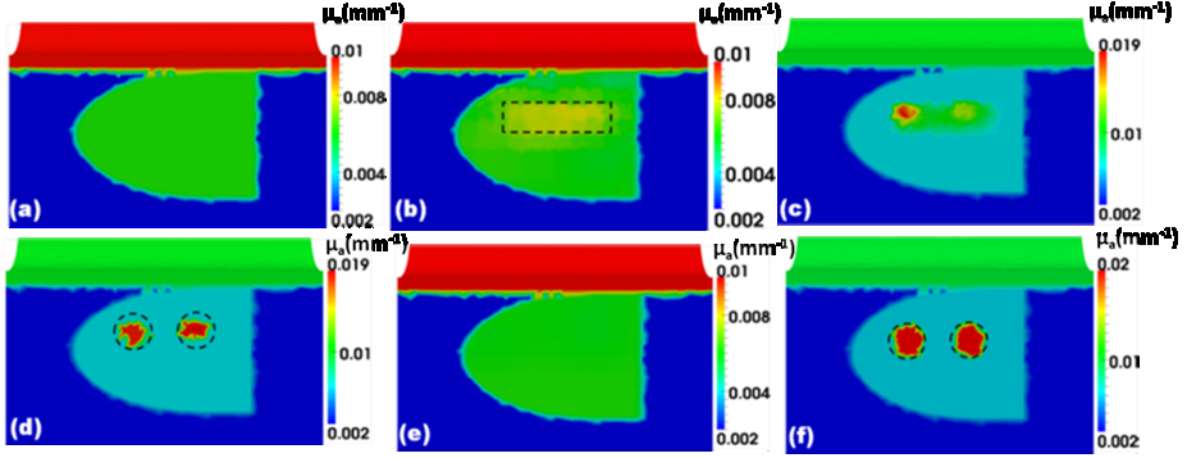


Figure 3: reconstructed μ_a values in mm^{-1} using different reconstruction steps. The dotted circles indicate the real locations of the anomaly. Reconstructed image (a) after step 1 using HCM, (b) after step 2 using HCM; dotted rectangle indicates the suspicious location selected using FWHM, (c) after step 3 using HCM, (d) after step 4 using HCM. (e) Reconstructed image without any inclusions, but reconstructed using HCM. (f) Reconstructed image for the same case using a known hard prior for the inclusions.

2.3 Measurement system and data processing

Instrumentation

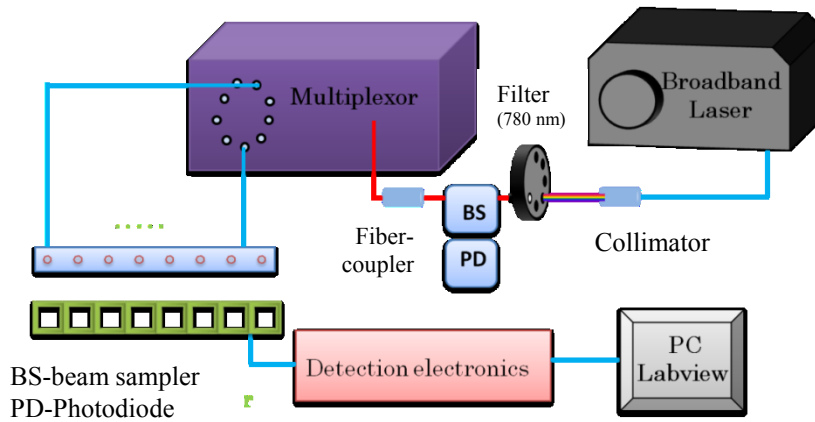


Figure 4: Instrumentation and probe setup utilized for laboratory phantom experiment. Eight sources and detectors were used for light delivery and detection.

For demonstrating HCM experimentally, we utilized the setup depicted in Fig. 4. A broadband pulsed laser source (SC-450, Fianium Inc., Eugene, Oregon) with a max output power of 40 mW (measured at the tip of an optical fiber) was utilized as the illumination source. Although the pulsed laser has a repetition rate of 20 MHz, due to the limited frequency response of the photodiodes, we still considered our system as a CW system. The laser output was collimated and fed through a filter wheel where a

desired wavelength of 780nm was selected. In order to calibrate the fluctuations from the laser source, a beam sampler (BS) was utilized, and a sample beam was fed into another photodiode (PD) for further calibration. The light was again coupled into another optical fiber and fed into a multiplexor. The multiplexor, as controlled by a computer, illuminated 8 locations on an optode probe sequentially. We employed silica optical fibers (core diameter of 600 μm) for light delivery.

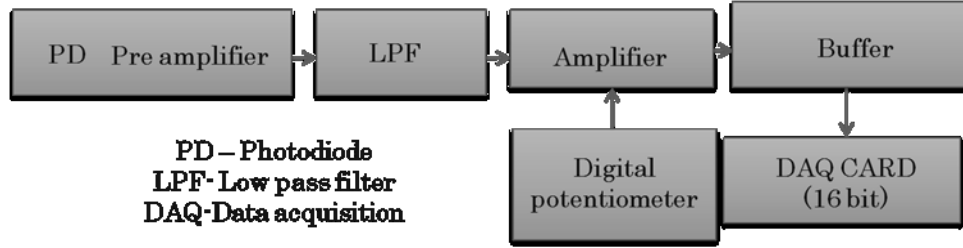


Figure 5: Flow chart depicting various stages of detection electronics utilized in proposed instrumentation

For the detection electronics (Fig. 5), we utilized photodiodes (OPT101, Burr-Brown Corp., Tucson, Arizona) to collect the diffused light. An analog low pass filter (LPF) was employed to filter out unwanted higher frequencies. Next, the electrical signal was amplified using an operational amplifier in the inverting mode. The operational amplifier's gain was controlled by changing the resistance of feedback resistor. For digital control of gain, a digital potentiometer was utilized such that the gain was controlled from the computer. Next, the electrical signal was further fed into a buffer amplifier which itself was an operational amplifier in non-inverting mode with unity gain. Finally, we utilized a National Instruments DAQ card with 16-bit resolution to convert analog signals into digital format and stored in the computer. The proposed instrument setup, including scanning mechanism, electrical gain, and data acquisition, was controlled using Labview software.

Experimental setup

Although in the computer simulations, we demonstrated our HCM using a multilayered model, we utilized a single layer phantom for experimental demonstration. We preferred a single layered phantom because of the complexity involved in the preparation of a multilayered phantom. Using a single layered phantom with an absorber inside, we skipped Step 1 in our reconstruction technique and directly started the reconstruction from step 2. The reason for skipping Step 1 was that it involved inducing the prior information; for this particular case, we did not use any prior information. The phantom setup is depicted in Fig. 6. A homogeneous liquid tissue-mimicking phantom was prepared by filling a container of dimensions of $15 \times 10 \times 10 \text{ cm}^3$ with 1% Intralipid solution. This solution served as the homogeneous background medium with an absorption coefficient (μ_a) of 0.1 cm^{-1} and reduced scattering coefficient (μ'_s) of 10 cm^{-1} . A spherical absorbers ($\mu_a = 0.3 \text{ cm}^{-1}$) of 1-cm diameter were placed at 1.5-cm distance around the center of an optode array which was placed from one side surface of the container, as shown in Fig. 6.

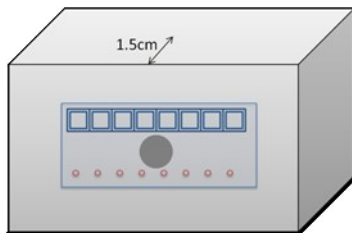


Figure 6: Experimental setup used in the laboratory phantom measurement. An optode probe has been placed on the side of the tank to avoid contact with the intralipid solution. An absorber has been placed 1.5 cm from the side of the tank within the Intralipid solution.

Experimental results

Panels in Fig. 7 provide overall comparisons among the reconstructed images that were obtained using the experimental setup given in Figs. 4-6. Figure 7(a) demonstrates the result obtained from the regular iterative DOT reconstruction technique. While this figure shows relatively good reconstruction in both location and size for the embedded absorber, we see very poor recovery in absorption contrast for the reconstructed object: the reconstructed value of μ_a was 0.012 cm^{-1} while the expected value was 0.03 cm^{-1} . As seen in Fig. 7(b), step 2 in our HCM is able to determine the probable location of the absorber; Figs. 7(c) and 7(d) show the gradual improvement in the contrast recovery. By the end, both location and absorption contrast of the embedded absorber were reconstructed much better to meet the expected values.

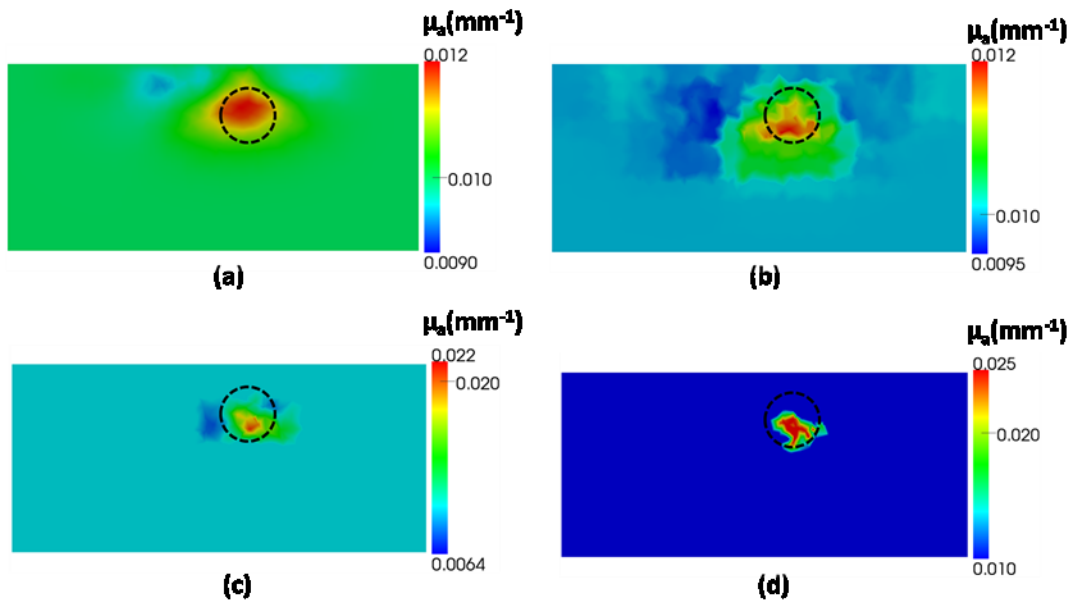


Figure 7: reconstructed μ_a values and maps in mm^{-1} (a) using regular iterative DOT reconstruction technique and HCM after (b) step 2, (c) step 3, and (d) step 4.

3. Key Research Accomplishments and Reportable Outcomes

Key research accomplishments:

- (1) We have shown the feasibility of TRUS-DOT through computer simulations and laboratory phantom experiments.
- (2) We have designed a TRUS-compatible, DOT-based image system (780nm), in which the photo diodes were placed on the trans-rectal probe. Optical signals were recorded and used for estimating the absorption coefficient.
- (3) We validated the system using laboratory phantoms. For improved image reconstruction, we have also developed a hierarchical clustering method (HCM) to improve the accuracy of image reconstruction with limited prior information.

Reportable outcomes:

- (1) Peter LeBoulluec, Hanli Liu, and Baohong Yuan, "A cost-efficient frequency-domain photoacoustic imaging system," Am. J. Phys. Vol. 81, 712 (2013); doi: 10.1119/1.4816242
- (2) Venkaiah C. Kavuri and Hanli Liu, "Development of multispectral transrectal ultrasound compatible near infrared imaging system for early detection of prostate cancer," SPIE, Photonics West, BiOS Biomedical Optics Symposium, paper 8578-57, Feb. 2-7, 2013, San Francisco, California.

4. Conclusions

As mentioned in Section 1, we have modified our original goals or ideas by developing transrectal ultrasound-guided diffuse optical tomography (TRUS-DOT) for improved prostate cancer imaging. In this report, we have shown the feasibility of TRUS-DOT through computer simulations and laboratory phantom experiments. Specifically, we have designed a TRUS-compatible, DOT-based image system (780nm), in which the photo diodes were placed on the trans-rectal probe. Optical signals were recorded and used for estimating the absorption coefficient. We validated the system using laboratory phantoms. For improved image reconstruction, we have also developed a hierarchical clustering method (HCM) to improve the accuracy of image reconstruction with limited prior information.

For the extended period of funding (till March 31, 2014, which has been approved), we have following modified Statement of Work (SOW) to complete:

Task 1: We will make more tissue phantoms for TRUS-compatible imaging experiments by using gelatin materials mixed with blood and intralipid. We will perform the TRUS-DOT imaging measurements with the prostate-shaped phantoms that simulate cancerous tissues.

Task 2: We will characterize the quality of reconstructed TRUS-DOT images, including image resolutions, position errors of the given simulated tumors, and quantification accuracy of the physiological parameters of the simulated tumor tissues.

In the meantime, we will publish our results in peer-reviewed journals.

5. References

1. P. Leboulluec, B. Yuan, and H. Liu, "A compact and cost-efficient frequency-domain photoacoustic imaging technique," *American Journal of Physics*, in press 2013.
2. S. Telenkov, A. Mandelis, B. Lashkari, and M. Forcht, "Frequency-domain photothermoacoustics: Alternative imaging modality of biological tissues," *Journal of Applied Physics* **105**, 102029, (2009).
3. G. Xu, D. Piao, C. H. Musgrove, C. F. Bunting, and H. Dehghani, "Trans-rectal ultrasound-coupled near-infrared optical tomography of the prostate, part I: simulation," *Optics express* **16**, 17484-17504 (2008).
4. P. K. Yalavarthy, B. W. Pogue, H. Dehghani, C. M. Carpenter, S. Jiang, and K. D. Paulsen, "Structural information within regularization matrices improves near infrared diffuse optical tomography," *Optics Express* **15**, 8043-8058 (2007).
5. H. Dehghani, B. W. Pogue, J. Shudong, B. Brooksby, and K. D. Paulsen, "Three-dimensional optical tomography: resolution in small-object imaging," *Appl. Opt.* **42**, 3117-3128 (2003).
6. H. Dehghani, M. E. Eames, P. K. Yalavarthy, S. C. Davis, S. Srinivasan, C. M. Carpenter, B. W. Pogue, and K. D. Paulsen, "Near infrared optical tomography using NIRFAST: Algorithm for numerical model and image reconstruction," *Communications in numerical methods in engineering* **25**, 711-732 (2009).

A cost-efficient frequency-domain photoacoustic imaging system

Peter LeBoulluec, Hanli Liu, and Baohong Yuan

Citation: *Am. J. Phys.* **81**, 712 (2013); doi: 10.1119/1.4816242

View online: <http://dx.doi.org/10.1119/1.4816242>

View Table of Contents: <http://ajp.aapt.org/resource/1/AJPIAS/v81/i9>

Published by the American Association of Physics Teachers

Additional information on Am. J. Phys.

Journal Homepage: <http://ajp.aapt.org/>

Journal Information: http://ajp.aapt.org/about/about_the_journal

Top downloads: http://ajp.aapt.org/most_downloaded

Information for Authors: <http://ajp.dickinson.edu/Contributors/contGenInfo.html>

ADVERTISEMENT



American Association of **Physics Teachers**

Explore the **AAPT Career Center** –
access hundreds of physics education and
other STEM teaching jobs at two-year and
four-year colleges and universities.

<http://jobs.aapt.org>



APPARATUS AND DEMONSTRATION NOTES

The downloaded PDF for any Note in this section contains all the Notes in this section.

Frank L. H. Wolfs, *Editor*

Department of Physics and Astronomy, University of Rochester, Rochester, New York 14627

This department welcomes brief communications reporting new demonstrations, laboratory equipment, techniques, or materials of interest to teachers of physics. Notes on new applications of older apparatus, measurements supplementing data supplied by manufacturers, information which, while not new, is not generally known, procurement information, and news about apparatus under development may be suitable for publication in this section. Neither the *American Journal of Physics* nor the Editors assume responsibility for the correctness of the information presented.

Manuscripts should be submitted using the web-based system that can be accessed via the *American Journal of Physics* home page, <http://ajp.dickinson.edu> and will be forwarded to the ADN editor for consideration.

A cost-efficient frequency-domain photoacoustic imaging system

Peter LeBoulluec, Hanli Liu, and Baohong Yuan^{a)}

Department of Bioengineering, The University of Texas at Arlington, Arlington, Texas 76019 and Joint Biomedical Engineering Program, The University of Texas at Arlington and The University of Texas Southwestern Medical Center at Dallas, Texas 75390

(Received 14 September 2010; accepted 8 July 2013)

Photoacoustic (PA) imaging techniques have recently attracted much attention and can be used for noninvasive imaging of biological tissues. Most PA imaging systems in research laboratories use the time domain method with expensive nanosecond pulsed lasers that are not affordable for most educational laboratories. Using an intensity modulated light source to excite PA signals is an alternative technique, known as the frequency domain method, with a much lower cost. In this paper, we describe a simple frequency domain PA system and demonstrate its imaging capability. The system provides opportunities not only to observe PA signals in tissue phantoms but also to acquire hands-on skills in PA signal detection. It also provides opportunities to explore the underlying mechanisms of the PA effect. © 2013 American Association of Physics Teachers. [<http://dx.doi.org/10.1119/1.4816242>]

I. INTRODUCTION

Optical imaging of cancer has been intensively studied in recent years due to its unique and high sensitivity to endogenous and exogenous tumor contrast.^{1,2} These optical techniques are usually limited either in penetration depth, e.g., a few hundred of microns for optical microscopy, or in spatial resolution, e.g., a few millimeters for optical diffuse optical tomography (DOT).¹⁻³ Obviously, a tradeoff exists between the imaging depth and spatial resolution.⁴ To overcome this limitation, ultrasound techniques have been combined with optical approaches, yielding various diagnostic techniques such as photoacoustic (PA) imaging.⁴ Using PA techniques, the ratio of imaging depth to spatial resolution can reach values up to about 100, which is ~ 10 times higher than what can be achieved with conventional DOT. PA techniques can potentially be used for imaging cancers in human breast, prostate, skin, thyroid, neck, head, and others areas.⁴ PA techniques provide optical contrast, which is usually much more sensitive to functional and molecular information of the tissue than ultrasound techniques, making it possible to measure the concentrations of total hemoglobin, oxy- and deoxy-hemoglobin, and specific molecules regulating tumor growth and metastasis.^{4,5} Compared with pure optical imaging methods, such as DOT, PA techniques have much higher spatial resolution and similar imaging depth.^{4,5} The basic

mechanism of the PA effect can be briefly explained as follows: (1) tissue absorbs the energy of light illumination; (2) the absorbed energy leads to a local temperature rise in the tissue; and (3) a pressure or sound wave, called the PA signal, is generated due to the thermoelastic effect.⁴

Most PA imaging systems in large research laboratories use a nanosecond pulsed laser with high pulse energy. A short light pulse avoids energy loss due to thermal energy diffusion before the generation of PA signals, which is known as thermal confinement.⁶ A nanosecond pulsed laser with high pulse energy typically costs tens of thousands of dollars and is usually positioned on a large optical table. Low cost and compact PA imaging techniques that do not rely on nanosecond pulsed laser systems are useful for educational and research laboratories with limited resources and for global healthcare.⁷⁻¹¹ In this study, we have developed a frequency-domain PA (FD-PA) imaging system by using an inexpensive laser diode, a conventional single element ultrasound transducer, and a lock-in amplifier to improve the signal-to-noise ratio.¹²⁻¹⁶ The theory and the experimental implementation of FD-PA have been extensively described in the literature.^{8,10,11,17} A simple, compact, and cost efficient FD-PA imaging system is an excellent teaching and research tool for educators and researchers. It allows students and the general public to understand the underlying mechanisms of the PA effect and its applications, such as cancer imaging.

II. FUNDAMENTAL THEORY OF FREQUENCY-DOMAIN PHOTOACOUSTICS

The wave equation used to quantify photoacoustic pressure is usually expressed as follows:

$$\left(\nabla^2 - \frac{1}{v^2} \frac{\partial^2}{\partial t^2}\right)P = \frac{-\beta}{C_P} \frac{\partial H}{\partial t}, \quad (1)$$

where P represents the photoacoustic signal, H is the laser heating function, v is the speed of sound, β is the thermal expansion coefficient, and C_P is the heat capacity per unit mass at constant pressure of the irradiated medium. In the

frequency domain, the laser intensity is usually modulated as a sinusoidal function with frequency f . Assuming the amplitude of the modulated intensity is I_0 , the heating function can be expressed as:

$$H = \mu_a I_0 \exp(-i\omega t), \quad (2)$$

where $\omega = 2\pi f$ and μ_a is the absorption coefficient of the medium, which is usually proportional to the absorber concentration in the sample. When considering an infinitely long and optically thin planar or cylindrical absorber, the generated PA waves in the frequency-domain can be represented by

$$P = \frac{i\mu_a \beta I_0 v l}{2C_P} \left[\frac{\text{sinc}(\hat{q})}{\sin(\hat{q}) + i\hat{\rho}\hat{v} \cos(\hat{q})} \right] \exp(-i\hat{q}\hat{t}), \quad (\text{planar absorber}) \quad (3)$$

$$P = \frac{i\mu_a \beta I_0 v a}{C_P} \left[\frac{J_1(\hat{q})H_0^{(1)}(\hat{v}\hat{r}\hat{q})/\hat{q}}{J_1(\hat{q})H_0^{(1)}(\hat{v}\hat{q}) - \hat{\rho}\hat{v}J_0(\hat{q})H_1^{(1)}(\hat{v}\hat{q})} \right] \exp(-i\hat{q}\hat{t}), \quad (\text{cylindrical absorber}) \quad (4)$$

where l is the thickness of the slab, a is the radius of the cylinder, and \hat{r} is the radial coordinate. J_0 and J_1 are the zeroth and first-order Bessel functions, respectively. $H_0^{(1)}$ and $H_1^{(1)}$ represent the zeroth- and first-order Hankel functions, respectively. \hat{q} is the dimensionless frequency and \hat{t} is the dimensionless time. For a slab, $\hat{q} = \omega l/2v$ and $\hat{t} = 2v(t - \frac{z-1/2}{v})$. For a cylinder, $\hat{q} = \omega a/v$ and $\hat{t} = vt/a$. $\hat{\rho} = \rho_{in}/\rho_{out}$ and $\hat{v} = v_{in}/v_{out}$ are the dimensionless density and speed-of-sound parameters, respectively. The subscripts “in” refers to inside the absorber and “out” refers to outside the absorber. For a small spherical absorber with radius a , the PA wave can be expressed as

$$P = \frac{i\mu_a \beta I_0 v a}{C_P(r/a)} \left[\frac{[\sin(\hat{q}) - \hat{q} \cos(\hat{q})]/\hat{q}^2}{(1 - \hat{\rho})(\sin(\hat{q})/\hat{q}) - \cos(\hat{q}) + i\hat{\rho}\hat{v} \sin(\hat{q})} \right] \times \exp(-i\hat{q}\hat{t}), \quad (5)$$

where $\hat{q} = \omega a/v$ and $\hat{t} = (\frac{v}{a})(t - \frac{r-a}{v})$.

Using Eqs. (3)–(5), the following can be concluded about the strength of the FD-PA signal: (1) it is a sinusoidal function of time with the same frequency ω as that of the modulated light; (2) it is proportional to the optical absorption coefficient μ_a of the medium; (3) it is proportional to the amplitude of the modulated intensity I_0 ; and (4) it depends on the modulation frequency ω via \hat{q} .^{18,19} In this study, the sample setup can be assumed to be a cylindrical absorber, described by Eq. (4).

III. MEASUREMENT SYSTEM AND DATA PROCESSING

A. Measurement system

Figure 1 shows the experimental setup. A function generator (FG, Agilent 33120A, Agilent Tech) generates a sinusoidal voltage signal of frequency f and a synchronized TTL (Transistor-Transistor Logic) signal with the same frequency

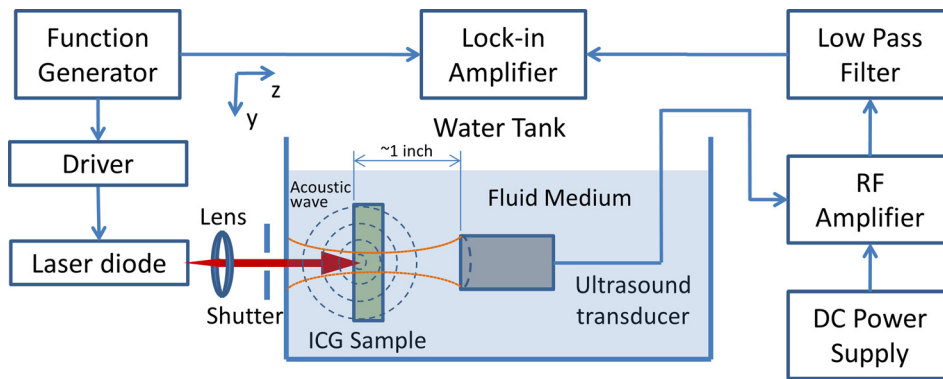


Fig. 1. The experimental setup used for PA imaging. The tank with the ICG sample is filled with either water or an intralipid solution. The function generator provides a sinusoidal voltage signal to the driver of the laser diode. A synchronized TTL signal is sent to the lock-in amplifier and serves as the reference signal. The laser diode emits a modulated light beam that is focused on the sample. A shutter is used to block the laser in order to measure the background noise. The modulated light is absorbed by the sample, causing the emission of PA waves, which are detected by the ultrasound transducer. The output voltage signal from the transducer is amplified, filtered, and sent to the lock-in amplifier.

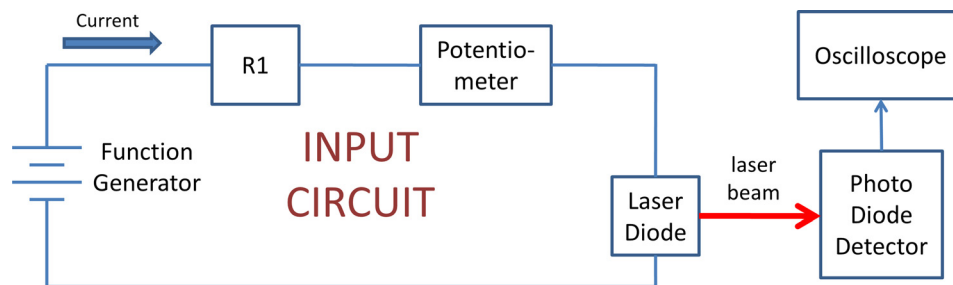


Fig. 2. Schematic of the modulation circuit used in our setup. The function generator provides DC and AC power to the circuit. The resistor and the potentiometer are chosen to provide a modulated current within the current range of the laser diode. The photodiode detector and oscilloscope are used to verify the modulation.

and a fixed phase shift. The sinusoidal signal is sent to a homemade circuit, shown in Fig. 2, to drive the laser diode (L785P100, Thorlabs). Thus, the laser intensity is modulated with the frequency f . The laser diode has a central wavelength of 785 nm and a power of ~ 100 mW when operating in DC mode. A lens is used to collimate the laser beam and a mechanical shutter is used to manually block the laser illumination to measure the background signal. The synchronized TTL signal from the FG is sent to a lock-in amplifier (LIA, SR844, Stanford Research Systems) and used as a reference signal. The sample and ultrasound transducer (UST, Olympus NDT, 1 in. inch focal length) are submerged into a transparent 10-gal tank (20 cm wide, 40 cm long, and 24 cm high), filled with either water or an intralipid solution. The sample used is an indocyanine green (ICG) aqueous solution, which is injected into a partially optically and acoustically transparent tube (MRE-095, Braintree Scientific) that is vertically positioned in the tank. The outer and inner diameters of the tube are 2.5 and 1.7 mm, respectively. The UST is focused on the sample. Both the lateral and axial sizes of the focal zone, normally measured in terms of the full width at half maximum (FWHM), depend on the central frequency of the UST. When the intensity-modulated laser reaches the optically absorbing sample, a PA wave is generated. The PA wave is detected and converted into a voltage signal by the UST and further amplified (ZFL-1000LN, Mini Circuits) and filtered (SLP-5+, Mini Circuits). A total gain of 40 dB is applied by using two identical amplifiers in series, driven by a DC power supply (BK Precision 1506). The low pass filter (SLP-5+, Mini Circuits) is not required because the LIA has a very narrow bandwidth. The processed PA signal is delivered to the LIA and the amplitude of the PA signal and the phase difference between the PA signal and the reference signal are displayed on the screen of the LIA.

Figure 2 shows the principle of the modulation circuit. By generating an AC signal with a DC offset, the FG can serve as a DC and AC power source. A resistor (R1) and a potentiometer are used to limit and control the current flowing into the laser diode, respectively. The laser diode has a typical threshold current of 35 mA. The DC offset of the FG is $V_{DC} = 2$ V and the AC peak-to-peak is $V_{AC} = 4$ V. The total resistance of R1 and the potentiometer is about 11 Ω . A photodiode (EOT, ET-2030 A) is used to verify the modulation of the laser intensity via an oscilloscope (2530B Digital Storage Oscilloscope, BK Precision).

B. Data processing

It is common that the LIA shows a background signal even when the laser is turned off or blocked. This background signal is mainly caused by electronic interference from the driving

signal generated by the FG. Fortunately, this background signal is independent of the location of the UST or the sample. A simple way to eliminate the effect of this background signal is to mathematically subtract it from the measured PA signal. Figure 3 schematically shows the relationship between the three signals, based on the amplitude and the phase measured with the LIA: (1) the measured signal, (2) the background signal, and (3) the PA signal. The angle between the vector representing each signal and the horizontal axis is the phase. The PA signal, vector (3) in Fig. 3, is the difference between the measured signal and the background signal. The magnitude of the PA signal is correlated with the optical absorption coefficient of the sample. All the calculations, image processing, and plotting were carried out using MATLAB (Mathworks), which is commonly used in engineering laboratories. Other software packages, such as MATHCAD, can be used as alternatives.

IV. RESULTS AND DISCUSSIONS

Before the PA measurements, the laser beam was positioned to be coaxial with the UST. The tank was filled with a 1% intralipid solution to simulate biological tissues. The absorption and scattering coefficients of the intralipid solution are 0.04 cm^{-1} and 8.4 cm^{-1} , respectively, as measured with an ISS Oximeter. The tube was filled with an ICG aqueous solution, with a concentration of 0.5 g/l, to simulate an absorbing target. ICG is a relatively weak fluorophore in the near infrared range with a quantum yield of $< \sim 1\%$ in aqueous media²⁰ and has been used as an optical absorber for PA imaging.²¹ The laser diode and the UST were mounted on the same translation stage and their relative position was thus fixed. By moving the translation stage, the PA signal distributions along the x axis and in the x-y plane were acquired. Although the coaxial setup between the laser beam and the UST is not required, it improves the signal-to-noise ratio.

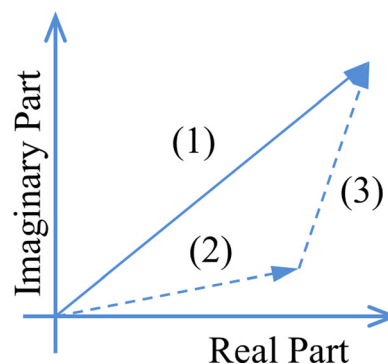


Fig. 3. The relation between the measured signal (vector 1), the background (vector 2), and PA (vector 3) signals.

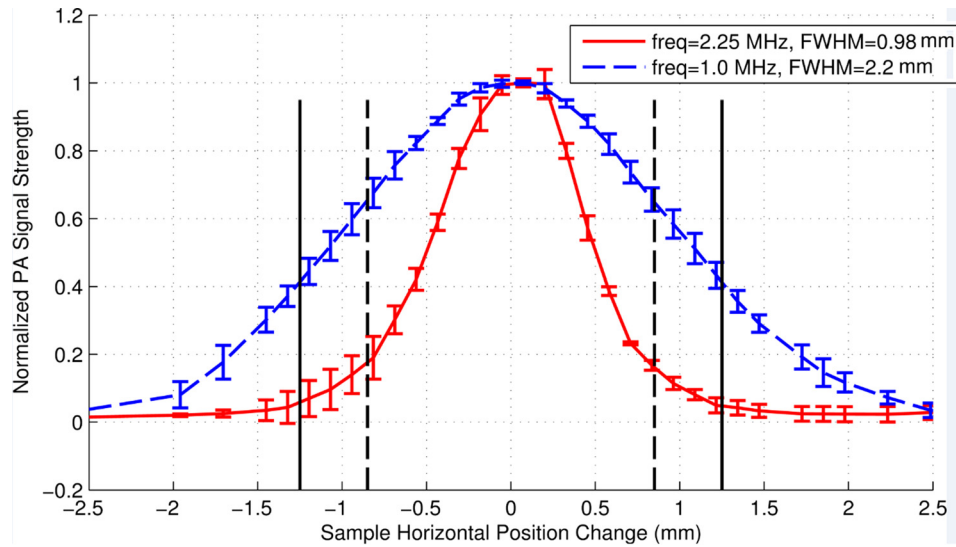


Fig. 4. The normalized PA signal strength as a function of the horizontal position of the sample relative to the co-axis of the laser beam and the UST. The data were obtained with a 1 MHz (dashed curve) and a 2.25 MHz (solid curve) UST. The dashed vertical lines show the inner diameters and the solid vertical lines show the outer diameters of the phantom tube that is filled with 0.5 g/l ICG solution at a depth of 1.9 mm in a 1% intralipid solution. The diameter of the collimated laser beam is ~ 1.0 mm. The error bars represent the standard deviation of 4 measurements.

Figure 4 shows the strength of measured PA signal as a function of the horizontal position of the tube relative to the axis of the laser beam and the UST. The dashed and solid vertical lines represent the inner and outer diameter of the tube, respectively. Clearly, the strength of the PA signals rise when the laser beam gradually moves into the tube region and fall when the laser beam moves away from the tube region. These results indicate that the highly absorbing ICG tube generates significant PA signals compared to the surrounding intralipid solution that has a much lower absorption coefficient. The FWHM of the PA data using the 1 MHz UST, shown in Fig. 4, is about 2.2 mm. It is larger than the inner diameter of the tube (1.7 mm) and the UST lateral size (1.3 mm) since the FWHM is mainly determined by the convolution of the profiles of the cross section of the tube and the lateral focal zone of the UST.

When the frequency of the UST is increased from 1 to 2.25 MHz, the FWHM of the UST's lateral focal zone is reduced from ~ 1.3 to ~ 0.72 mm. The PA spatial resolution can be thus improved by using a higher frequency UST. Figure 4 shows that the FWHM of the PA signal measured with the 2.25 MHz UST is 0.98 mm which is smaller than the 2.2 mm width measured with the 1 MHz UST. However, the

width is smaller than the tube size and the reason is unclear. One possible reason may be that the PA signal generated from regions close to the edge of the tube is too weak to be detected. Higher frequencies provide smaller focal sizes and higher spatial resolution. A UST with a central frequency between 1 and 10 MHz achieves an acceptable spatial resolution. At frequencies below 1 MHz, the resolution will be degraded. Frequencies above 10 MHz will also work but increases the cost and the complexity of the system.

When the distance between the left-side of the tank wall and the left outer surface of the tube, defined as the depth of the tube, increases, the strength of the PA signal decreases. This is a consequence of the reduction in the light intensity reaching the sample due to the scattering in the medium. The dependence of the strength of the PA signal on the thickness or depth of the medium is shown in Fig. 5.

Increasing the ICG concentration increases the absorption coefficient of the tube, which raises the PA signal strength. Figure 6 shows the peak strength of the PA signal as a function of the ICG concentration. The PA signal strength increases when the concentration is increased but appears to saturate at high ICG concentrations. This may indicate that the light cannot penetrate into a highly concentrated ICG

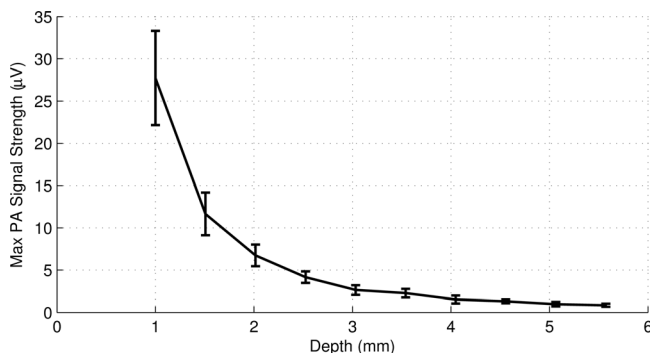


Fig. 5. The maximum PA signal strength as a function of the tube depth acquired with a 2.25 MHz UST in a 1% intralipid solution. The diameter of the laser beam is ~ 1.0 mm and the ICG concentration is 0.5 g/l. The error bars represent the standard deviation of 4 measurements.

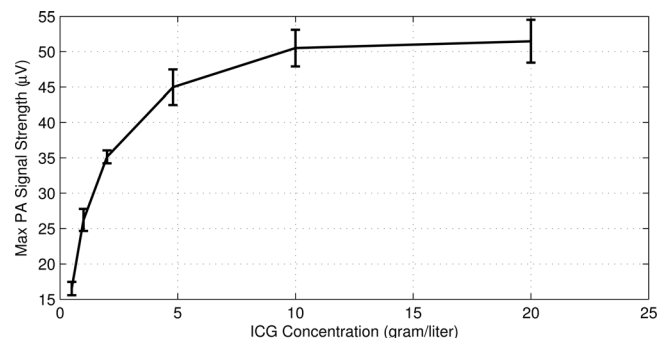


Fig. 6. The maximum PA signal strength as a function of the ICG concentration acquired with a 2.25 MHz UST in a 1% intralipid solution at a depth of 1.9 mm. The diameter of the collimated laser beam is ~ 1.0 mm. The error bars represent the standard deviation of 5 measurements.

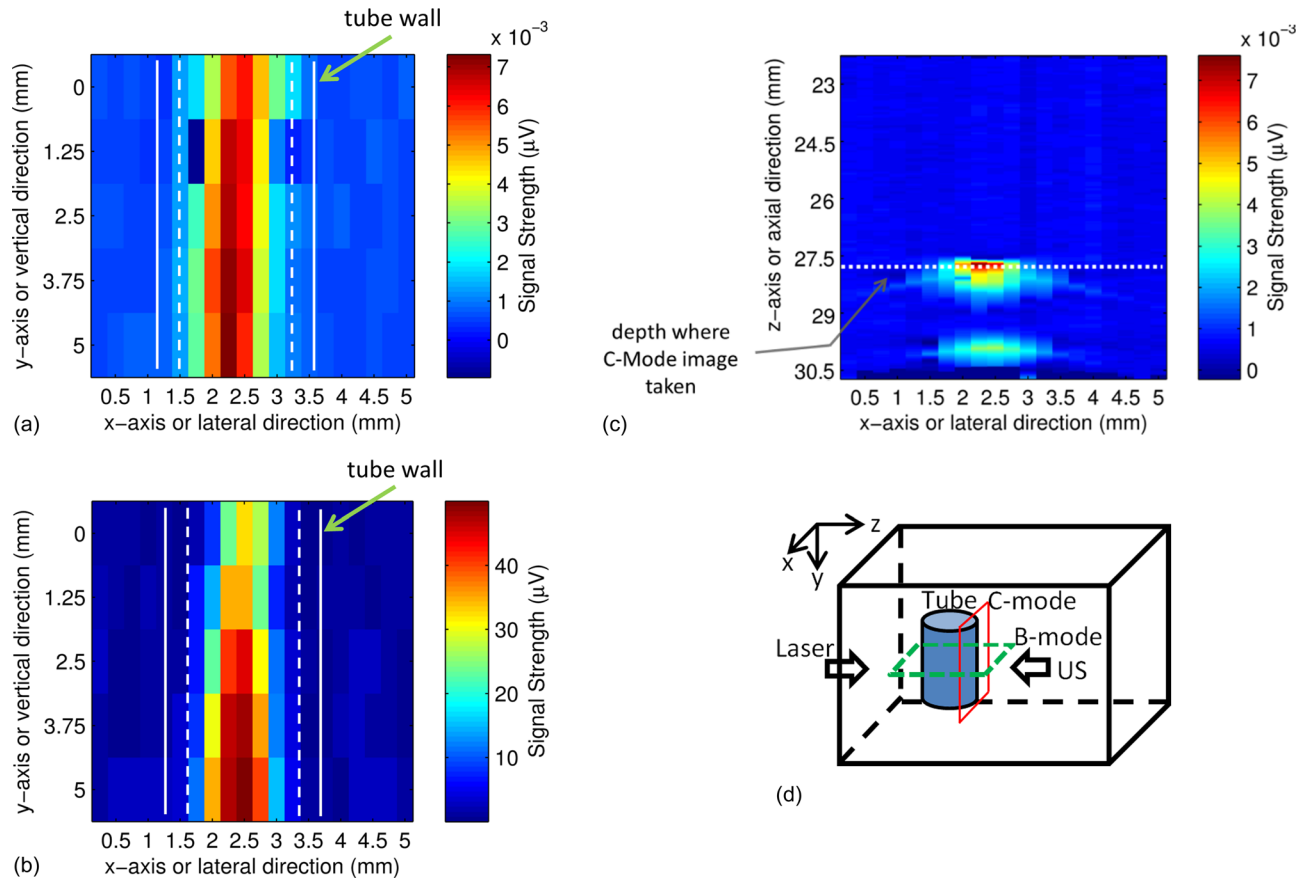


Fig. 7. (a) A C-mode ultrasound image and (b) a C-mode PA image of the ICG filled tube. The UST frequency is 2.25 MHz, the ICG concentration is 2 g/l, and the intralipid concentration is 1%. (c). An ultrasound B-mode image showing the cross section of the same ICG filled tube. The white dotted line indicates the depth of the C-mode images in (a) and (b). Note that the depth of zero in this figure is the surface of the UST, which is different from the definition of the tube depth). (d) A diagram to show the B-mode and C-mode imaging planes. The B-mode image is parallel to the x-z plane and the C-mode is parallel to the x-y plane (close to the right-side edge of the tube).

solution due to the large absorption coefficient, suggesting that the light absorption is confined to a limited region of the ICG solution.

Figures 7(a) and 7(b) show two-dimensional (2D) ultrasound and PA images of the tube in the x-y plane (C-mode, see Fig. 7(d) for the coordinates and the imaging plane). The ultrasound image was obtained with the same UST using the conventional pulse-echo method. The UST was connected to a pulse-generator-receiver (5073PR pulser/receiver, Olympus) and the reflected ultrasound data was acquired with the oscilloscope. The UST was raster scanned in the x-y plane. The laser was turned off because it is not used in ultrasound imaging. The reflected ultrasound echo signal at each location, also called the A-line, included the acoustic information along the z direction. After scanning the x-y plane, all A-lines can be used to construct a 3D image of the tube. Figures 7(a) shows a 2D image in the x-y plane, the so-called a C-mode ultrasound image, at a depth indicated by the white line in Fig. 7(c). Figure 7(c) shows a 2D image in the x-z plane, the so-called a B-mode ultrasound image, representing the cross section of the tube. The PA image shown in Fig. 7(b) was obtained with the system described in Fig. 1. This system does not have the capability to resolve the PA signal along z direction because the laser diode is continuously modulated. This is one disadvantage of the PA technique compared with the time-domain method. Therefore, only a 2D image in the x-y plane is shown in Fig. 7(b).

The data points shown in Figs. 7(a) and 7(b) were obtained by raster scanning the UST/laser system in the x-y plane. The step sizes in the lateral (x) direction and in the vertical (z) direction were 0.5 mm and 1.25 mm, respectively. Each rectangle represents the intensity of a single measurement. The two solid and dashed white vertical lines represent the outer and inner diameter of the tube, respectively. The average FWHM of the ultrasound image shown in Fig. 7(a) is about 0.98 mm, which is smaller than the inner diameter of the tube. Figure 7(b) shows the corresponding PA image in the x-y plane. The image clearly shows the tube with optical (absorption) contrast. The average FWHM is about 0.88 mm, which is also smaller than the inner diameter of the tube for reasons that are not clear.

Figure 7(c) shows the ultrasound image of the cross-section of the tube. To be consistent with conventional ultrasound imaging rules, zero depth in Fig. 7(c) is defined as the surface of the UST because that is the location where the ultrasound pulses are generated; note that this is different from the definition of the tube depth. The two bright areas show the two boundaries of the tube. Note that the inner boundaries of the tube cannot be resolved from this image due to the limited resolution of the UST (2.25 MHz). The dotted horizontal line in Fig. 7(c) indicates the depth of the ultrasound C-mode image shown in Fig. 7(a). Clearly, the ultrasound image shows the boundaries between the tube and the surrounding medium.

Table I. The major components of the PA system and their features, costs, and possible substitutes. The listed prices are for guidance only.

Item	Model	Feature	Cost (USD)	Substitutes
Lock-in amplifier	SRS 844	Broadband 200 MHz	~\$8,000	Regular LIA, <\$2000
Function generator	Agilent 33120 A	Multiple function and 20 MHz bandwidth	~\$1600	Regular FG, <\$1000
Focused ultrasound transducer	Olympus-NDT V314-SU-F	Point focused, NA=0.375	~\$350	Other focused USTs with a central frequency between 1 and 10 MHz and reasonable sensitivity
Laser diode	Thorlabs L785P100	785 nm and 100 mw CW	~\$40	Other laser diodes with power ~100 mw
RF amplifiers (2x)	Minicircuits ZFL-1000LN	Wideband, 0.1-1000 MHz	~\$178 (2x at \$89 each)	Other RF amplifiers with a gain ~40 dB
Low pass filter (not required)	Minicircuits SLP-5+	Cutoff at 5 MHz	~\$35	Other low pass filters with an appropriate cutoff frequency

V. COST AND COMPACTNESS ANALYSES

Table I shows the general costs, features, and possible substitutes of the major components of the current PA system. The cost of the system is dominated by the cost of the LIA and the FG although lower cost LIAs and FGs could be adopted. Clearly, the cost of a FD-PA imaging system is much less expensive than that of a time-domain imaging system. The cost of the MATLAB software is not included in Table I. A student version of MATLAB is relatively cheap but other free or relatively inexpensive software packages can be used as alternatives. All components of the FD-PA system are compact. Although we have not attempted to reduce the overall size of our setup in the current study, it is possible to integrate the entire system into a small and portable box by replacing the FG and LIA with a small, customized circuit board. It will be extremely difficult for a time-domain PA system to achieve the same compactness.

VI. CONCLUSIONS

A FD-PA imaging system was designed and its imaging capability was demonstrated with tissue-like phantoms. The imaging principle and data processing method were discussed. The measured PA signal strength depends on the absorption coefficient, the depth of the target, and the modulated light intensity of the laser diode. Appropriate processing of the measured PA data and background interference is an important key to correctly display the PA images. The lateral spatial resolution of PA images is dependent on the ultrasound frequencies and focal sizes of the ultrasound transducers. Although the current system has a low axial resolution due to the adopted ultrasound transducer, it can be significantly improved by using a high numerical aperture ultrasound transducer or by adopting a frequency-swept technique.⁹ The FD-PA imaging system is cost effective compared to a time-domain imaging system.

ACKNOWLEDGEMENTS

The authors acknowledge the funding support from DOD (W81XH-11-1-0231) and partially from NIH (7R15EB012312-02), CPRIT (RP120052), NSF (CBET-1253199) and seed grant of Research Enhancement Program from the University of Texas at Arlington.

^{a)}Author to whom correspondence should be addressed. Electronic mail: baohong@uta.edu

¹A. Corlu, R. Choe, T. Durduran, M. A. Rosen, M. Schweiger, S. R. Arridge, M. D. Schnall, and A. G. Yodh, "Three-dimensional in vivo fluorescence diffuse optical tomography of breast cancer in humans," *Opt. Express* **15**, 6696–6716 (2007).

²J. Culver, W. Akers, and S. Achilefu, "Multimodality molecular imaging with combined optical and SPECT/PET modalities," *J. Nucl. Med.* **49**, 169–172 (2008).

³D. M. McDonald and P. L. Choyke, "Imaging of angiogenesis: from microscope to clinic," *Nature Med.* **9**, 713–725 (2003).

⁴L. V. Wang, "Multiscale photoacoustic microscopy and computed tomography," *Nature Photon.* **3**, 503–509 (2009).

⁵L. H. V. Wang, "Ultrasound-mediated biophotonic imaging: A review of acousto-optical tomography and photo-acoustic tomography," *Dis. Markers* **19**, 123–138 (2004).

⁶M. Xu and L. Wang, "Photoacoustic imaging in biomedicine," *Rev. Sci. Instrum.* **77**, 041101 (2006).

⁷K. Maslov and L. V. Wang, "Photoacoustic imaging of biological tissue with intensity-modulated continuous-wave laser," *J. Biomed. Opt.* **13**, 024006 (2008).

⁸M. Euler, "Hands-on resonance-enhanced photoacoustic detection," *Phys. Teach.* **39**, 406–409 (2001).

⁹S. Telenkov, A. Mandelis, B. Lashkari, and M. Forcht, "Frequency-domain photoacoustics: Alternative imaging modality of biological tissues," *J. Appl. Phys.* **105**, 102029 (2009).

¹⁰W. F. Rush and J. E. Heubler, "Photoacoustic effect demonstration," *Am. J. Phys.* **50**, 669 (1982).

¹¹M. Euler, K. Niemann, and A. Muller, "Hearing light," *Phys. Teach.* **38**, 356–358 (2000).

¹²P. A. Temple, "An introduction to phase sensitive amplifiers: An inexpensive student instrument," *Am. J. Phys.* **43**, 801–807 (1975).

¹³E. Wolfson, "The lock-in amplifier: A student experiment," *Am. J. Phys.* **59**, 569–572 (1991).

¹⁴J. H. Scofield, "Frequency-domain description of a lock-in amplifier," *Am. J. Phys.* **62**, 129–133 (1994).

¹⁵S. K. Sengupta, J. M. Farnham, and J. E. Whitten, "A simple low-cost lock-in amplifier for the laboratory," *J. Chem. Educ.* **82**, 1399–1401 (2005).

¹⁶K. Edmondson, S. Agoston, and R. Ranganathan, "Impurity level lifetime measurements using a lock-in amplifier," *Am. J. Phys.* **64**, 787–791 (1996).

¹⁷F. A. McDonald, "Photoacoustic effect and the physics of waves," *Am. J. Phys.* **48**, 41–47 (1980).

¹⁸M. I. Khan, T. Sun, and G. J. Diebold, "Photoacoustic waves generated by absorption of laser radiation in optically thin cylinders," *J. Acoust. Soc. Am.* **94**, 931–940 (1993).

¹⁹L. Wang, *Photoacoustic Imaging and Spectroscopy* (CRC Press, Boca Raton, 2009).

²⁰T. J. Russin, E. I. Altinoglu, J. H. Adair, and P. C. Eklund, "Measuring the fluorescent quantum efficiency of indocyanine green encapsulated in nanocomposite particulates," *J. Phys. Condens. Matter* **22**, 334217 (2010).

²¹C. Kim, C. Favazza, and L. H. V. Wang, "In vivo photoacoustic tomography of chemicals: High-resolution functional and molecular optical imaging at new depths," *Chem. Rev.* **110**, 2756–2782 (2010).